remote sensing

MDPI

Article

A Fast High-Resolution Imaging Algorithm for Helicopter-Borne Rotating Array SAR Based on 2-D Chirp-Z Transform

Mengyi Qin [1], Dong Li [1,2,*], Xianhui Tang [1], Cao Zeng [3], Wenjun Li [4] and Liying Xu [4]

[1] School of Microelectronics and Communication Engineering, Chongqing University, Chongqing 400044, China
[2] Center of Communication and Tracking Telemetering Command, Chongqing University, Chongqing 400044, China
[3] National Laboratory of Radar Signal Processing, Xidian University, Xian 710071, China
[4] Shanghai Satellite Engineering Research Institute, Shanghai 200240, China
* Correspondence: dongli1983@cqu.edu.cn; Tel.: +86-151-2390-2987

Received: 18 April 2019; Accepted: 11 July 2019; Published: 13 July 2019

Abstract: In view of the azimuth resolution of the helicopter-borne rotating array synthetic aperture radar (RoASAR) depending on the azimuth reconstruction angle and the sector distortion caused by the azimuth Deramp processing, this paper proposes an efficient helicopter-borne RoASAR high-resolution imaging algorithm based on two-dimensional (2-D) chirp-z transform (CZT). First, the high-order Taylor series expansion is performed on the slant range, and the accurate 2-D spectral expression of the point target is obtained by using the method of series reversion (MSR). Based on that, the space-variant characteristics of the range cell migration (RCM) terms are analyzed. After that, the space-variant RCM and the sector distortion effect caused by the azimuth Deramp processing are removed by using efficient 2-D CZT, thereby increasing the azimuth reconstruction angle and improving the azimuth resolution. The proposed algorithm is efficient without the interpolation operation, and it is easy to implement in real-time. Finally, the simulations are provided to verify the effectiveness of the proposed algorithm.

Keywords: helicopter-borne rotating array SAR (RoASAR); chirp-z transform (CZT); method of series reversion (MSR)

1. Introduction

Helicopter-borne rotating array synthetic aperture radar (RoASAR) is a novel radar imaging model and system, which is installed and operated on a helicopter platform, where the radar antenna is set on a rigid support at the tip of the helicopter rotor. With the rotation of the rotor, the 360° area synthetic aperture radar (SAR) image around the helicopter platform can be obtained without the movement of the helicopter platform [1,2]. This advantage breaks through the shortcomings that traditional SAR imaging is restricted by the blind area at the front of the platform, and it has become a popular choice for helicopter-borne anti-collision systems.

In a complex low-altitude environment, the RoASAR system provides high-resolution SAR images in front of the helicopter platform, for full day, all-weather and real-time monitoring of potential threats [3–5]. In addition to that, the RoASAR system can perform continuous data acquisition for fixed targets. In recent years, some imaging methods for RoASAR have been proposed to obtain the SAR images. The time-domain correlation imaging method, such as the back-projection (BP) algorithm in [6], can be applied to any geometric configuration, but it is not suitable for real-time imaging processing due to its high computational complexity. In recent years, some improved fast time-domain

algorithms have also been proposed to reduce the computational complexity [7–9]. The sub-aperture imaging method proposed in [10] is of a low computational complexity but suffers from low azimuth resolution. To overcome the low-resolution shortcoming, the Omega-k imaging method is proposed in [11–13], but it also has the great computation burden caused by the Stolt interpolation operation, and it is only applicable to the small imaging area near the center of the scene due to the range of spatial-variant characteristics of the tangential velocity. To reduce the computational complexity, a novel imaging method based on the chirp-z transform (CZT) is proposed in [14,15], in which an efficient CZT is utilized to remove the range-azimuth coupling. However, this method ignores the azimuth sector distortion caused by azimuth Deramp operation. With the requirements of a real-time, high-resolution and imaging scene scope requirements of the helicopter system, a fast high-resolution RoASAR imaging algorithm still needs to be studied.

To overcome the aforementioned issues, an efficient high resolution RoASAR imaging algorithm based on the two-dimensional (2-D) CZT is proposed in this work. First, for the imaging geometric configuration, the system parameters design and azimuth resolution dependence characteristics on the beam width and rotor rigid length are analyzed. With the high-order Taylor expansion of the instantaneous slant range, the precise 2-D frequency analytic expression is derived by method of series reversion (MSR) [16]. Furthermore, according to the analysis on the range-dependent range cell migration (RCM), an efficient inverse CZT (ICZT) is developed to remove the spatial-variant features of RCM. SAR image distortion in azimuth direction caused by the azimuth Deramp operation is analyzed and compensated by the improved CZT, and a well-focused high-resolution SAR image is obtained. Compared with the existing methods, the proposed method is computationally efficient thanks to avoiding the interpolation operation and is of high azimuth resolution because the large azimuth reconstruction angle is utilized. Finally, simulation results and analysis verify the correctness and effectiveness of the proposed algorithm.

The rest of the paper is organized as follows. In Section 2, the geometric and signal model of airborne RoASAR system are introduced, and then, the system parameters design, azimuth angular resolution and slant range approximation are analyzed. Section 3 describes the proposed 2-D CZT imaging algorithm. In Section 4, simulation results and analysis are provided to verify the feasibility of the algorithm. Section 5 concludes the paper briefly.

2. Overall Analysis of the Helicopter-Borne RoASAR System

2.1. Geometric Model of the Helicopter-Borne RoASAR System

Figure 1a,b show the basic imaging geometric model of the RoASAR system, in which the antenna is integrated at the end of the inelastic rotary arm and mounted on the helicopter rotor shaft. In this configuration, the helicopter platform hovers at a height of H above the ground, the length of the rotating arm is r_a, and the angular velocity is ω. The irradiation direction of the radar is always perpendicular to the motion direction of the rotor end. Since the hovering state of the helicopter is regarded as a fixed platform, the lower angle θ is constant during the operation of the SAR.

Let t_a represent the azimuth slow time variable and assume that the beam is illuminated on the positive half of the X-axis at time $t_a = 0$. The coordinate of the reference point scatterer P in the scene can be expressed as $\left(r_p cos\theta_p,\ r_p sin\theta_p,\ 0\right)$, where r_p is the ground distance from the phase center of the antenna to the ground scatter P and $(r_a cos\theta_t,\ r_a sin\theta_t,\ H)$ is the instantaneous coordinate of the radar antenna phase center at the time t_a. The relationship between the angle and radius is

$$\begin{cases} \theta_t = \theta_0 + \omega t_a \\ r_p = r_a + Htan\theta \\ \theta_p = \omega t_p \end{cases}. \quad (1)$$

In the helicopter-borne RoASAR system, the positive half of the X-axis is selected as $t_a = 0$, and therefore, the corresponding initial angle is $\theta_0 = 0$. The instantaneous slant range from the radar antenna to the scatter P is expressed as

$$\begin{aligned} R\left(t_a; r_p\right) &= \sqrt{\left(r_a cos\theta_t - r_p cos\theta_p\right)^2 + \left(r_a sin\theta_t - r_p sin\theta_p\right)^2 + H^2} \\ &= \sqrt{r_a^2 + r_p^2 + H^2 - 2r_a r_p cos\left(\omega t_a - \omega t_p\right)} \end{aligned}. \tag{2}$$

Equation (2) is an exact expression of the slant range of RoASAR. Because of the cosine term in the slant range, it is difficult to obtain the accurate 2-D spectrum of the point target by using the principle of stationary phase (POSP), which brings difficulties to the design of an efficient frequency domain imaging algorithm. Therefore, some approximations must be made and the specific approximation process is given after the resolution and parameter analysis.

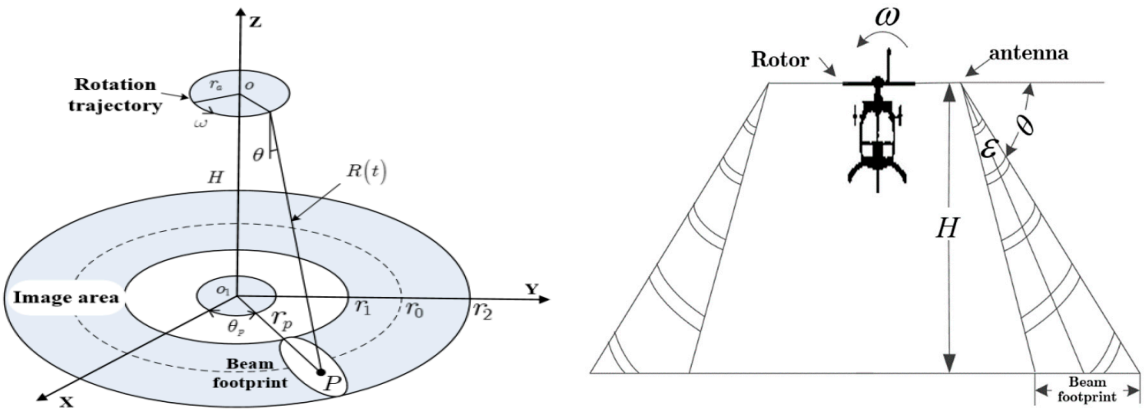

(**a**) (**b**)

Figure 1. Rotating array synthetic aperture radar (RoASAR) imaging geometric configuration. (**a**) RoASAR 3-D imaging geometric model. (**b**) RoASAR front view image.

2.2. Resolution Analysis of the Helicopter-Borne RoASAR System

The analysis of RoASAR resolution and related system parameters selection are discussed now. The range resolution ρ_r is determined by the bandwidth B_r of the transmitted signal, i.e., $\rho_r = c/(2B_r)$, and the corresponding ground resolution is $\Delta R_g = c/(2B_r sin\theta_{in})$, where θ_{in} is the incident angle. While the azimuth resolution of the helicopter-borne RoASAR is different from the traditional stripmap SAR, it depends on the size of the azimuth reconstruction angle, the helicopter rotor length and the wavelength. According to the matched filtering theory, the azimuth temporal resolution depends on the azimuth Doppler bandwidth B_a, i.e., $\Delta t_a = 1/B_a$. In RoASAR, bandwidth B_a is

$$B_a = 2 \cdot \frac{2v}{\lambda} cos(\varphi_{max}), \tag{3}$$

where φ_{max} is the maximal angle between the antenna and the center of the aperture, and v is the tangential velocity of antenna corresponding to the uniform rotation ω. From the diagram of the beam radiation trajectory for the target P in Figure 2, it is calculated that $\varphi_{max} = cos^{-1}\left(r_p \alpha / 2R_{amax}\right)$, where α is the azimuth reconstruction angle and R_{amax} is the maximum slant range corresponding to the point target in the reconstruction angle range. Therefore, the corresponding azimuth angular resolution is

$$\Delta\alpha = \omega \cdot \Delta t = \frac{\lambda}{4r_a cos(\varphi_{max})} = \frac{\lambda}{4r_a} \frac{2\sqrt{H^2 + r_p^2 + r_a^2 - 2r_a r_p cos(\alpha/2)}}{r_p \cdot \alpha}. \tag{4}$$

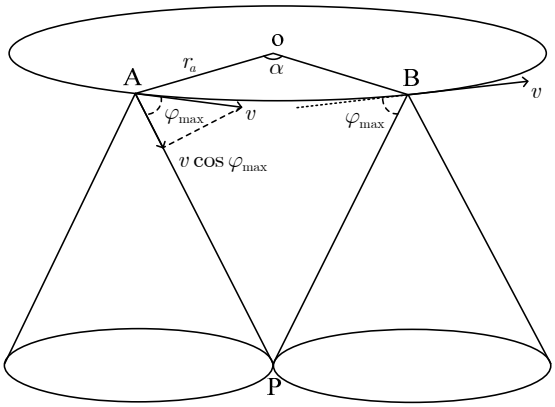

Figure 2. Diagram of the beam radiation trajectory for the target P.

It can be seen that the azimuth angle resolution is related not only to the ground distance of the target r_p, but also to the rotor length r_a, helicopter platform height H and azimuth reconstruction angle α. In Figure 3a, the result of the angular resolution at the reconstructed angle $\alpha = 70°$ and target ground distance $r_p = 2000$ m against the lengths of the rotor and the heights of the aircraft, is depicted. Figure 3b shows the azimuth angular resolution versus the reconstructed angle when the length of the rotor, the height of the aircraft and the target ground distance are fixed. Figure 3c shows the azimuth angular resolution versus the observation angle when the length of the rotor, the height of the aircraft and the target ground distance are fixed.

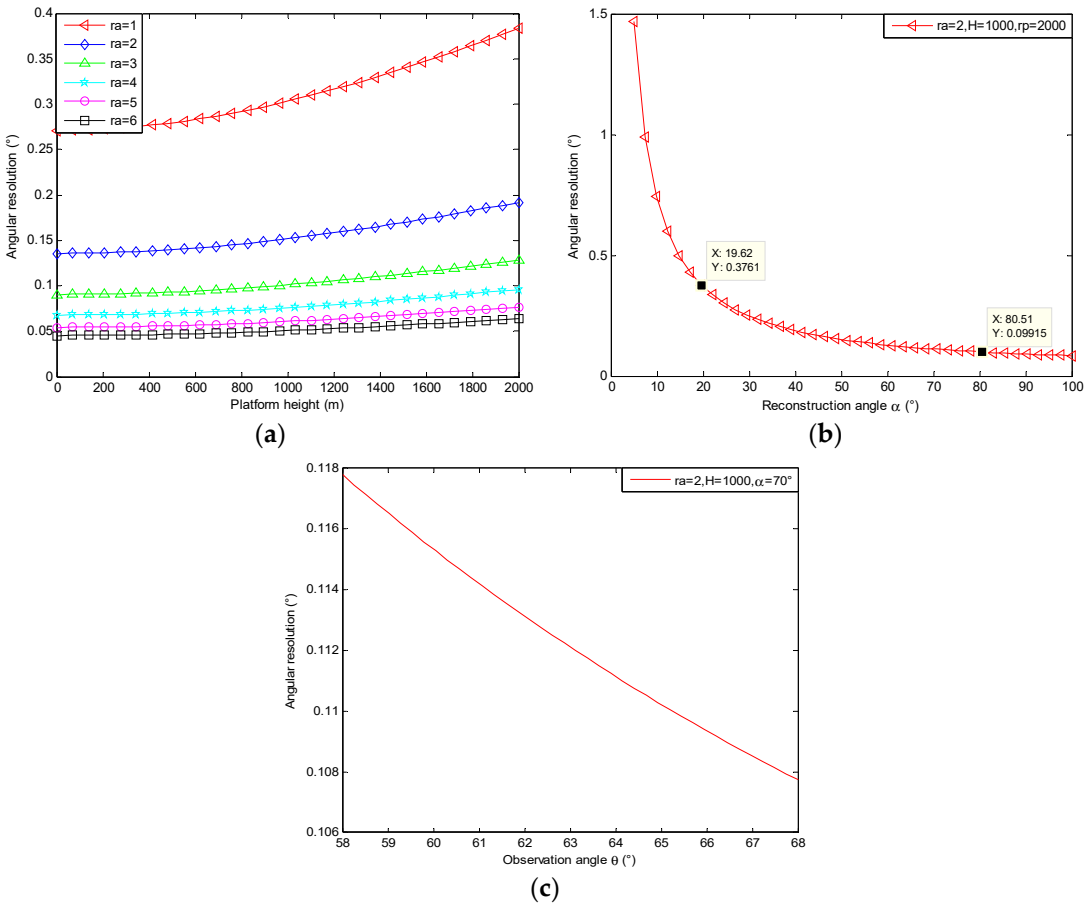

Figure 3. Variation curves of azimuth angular resolution. (**a**) Azimuth angular resolution varying with r_a and H. (**b**) Azimuth angular resolution varying with reconstruction angle α. (**c**) Azimuth angular resolution versus observation angle θ.

From Figure 3a, the azimuth angular resolution decreases with the increase in the height of the helicopter platform H. This is mainly because the increase in the height of the aircraft causes the component of the antenna linear velocity on the radar and target line of sight (LOS) to become smaller, decreasing the Doppler bandwidth. The longer the rotor length is, the higher the angular resolution is. The reason is that with the azimuth angle being fixed, the longer the rotor length is, the larger the synthetic aperture will be. Figure 3b shows that while other parameters are determined, the angular resolution of the target increases with an increase in reconstruction angle, which is consistent with the theoretical analysis.

Due to the physical limits of the helicopter's structure, the rotor length cannot be too long. To obtain higher azimuth resolution capability, it is hoped that the azimuth reconstructed angle can be as large as possible according to Figure 3b. However, the instantaneous slant range expression contains the cosine term, shown in Equation (2), which prevents the efficient frequency domain imaging algorithm developed. Therefore, some approximations need to be developed. For this problem, it is well-known that when the phase error introduced by the slant range approximation error ΔR is less than $\pi/2$, the influence on the imaging result can be ignored, i.e., $4\pi\Delta R/\lambda < \pi/2$. According to the aforementioned analysis, we set the system parameters of helicopter-borne RoASAR as the platform height $H = 1000$ m, rotor length $r_a = 2$ m, rotation angular velocity $\omega = 2\,\pi f = 15\ rad/s$, radar wavelength $\lambda = 0.03$ and the point target coordinates $(2000, 0, 0)$.

The detailed equations of second-order and fourth-order Taylor series expansion of the instantaneous slant range are developed in Appendix A (A9) and (A10), respectively. Under this case, Figure 4a,b show the approximated errors introduced by the second-order and fourth-order Taylor series expansion. It can be seen from Figure 4 that, in order to produce a well-focused image, the azimuth reconstruction angle can only be taken in the range between $-27°$ and $+27°$, while the range of the reconstruction angle can be reached between $-55°$ and $+55°$, when the slant range is expanded as the fourth Taylor series. Therefore, in this work, slant range is expanded as a fourth-order Taylor series.

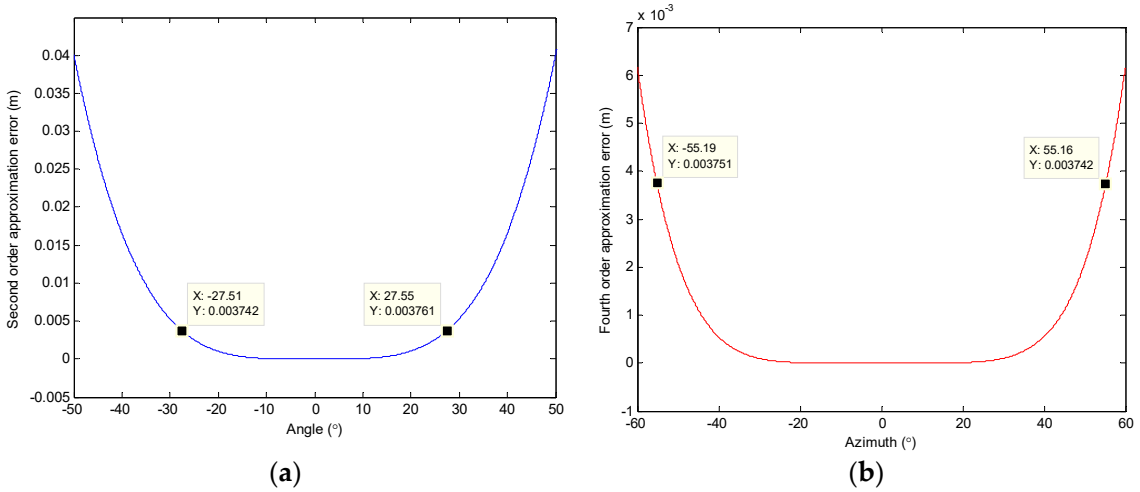

(**a**) (**b**)

Figure 4. Instantaneous slant range approximation error. (**a**) Second-order approximation. (**b**) Fourth-order approximation.

The slant range in Equation (2) is expanded as a fourth-order Taylor series, and the higher order terms are ignored, and two-way slant range now is

$$\begin{aligned} 2R\left(t_a;r_p\right) &\approx 2\sqrt{r_a^2+r_p^2+H^2-2r_ar_p\left(1-\frac{\omega^2\left(t_a-t_p\right)^2}{2}+\frac{\omega^4\left(t_a-t_p\right)^4}{24}\right)} \\ &= 2\sqrt{R_p^2+r_ar_p\omega^2\left(t_a-t_p\right)^2-\frac{r_ar_p\omega^4}{12}\left(t_a-t_p\right)^4} \\ &\approx 2R_p+\frac{r_ar_p\omega^2}{R_p}\left(t_a-t_p\right)^2-\left(\frac{r_ar_p\omega^4}{12R_p}+\frac{r_a^2r_p^2\omega^4}{4R_p^3}\right)\left(t_a-t_p\right)^4 \\ &= R_0+k_2\left(t_a-t_p\right)^2+k_4\left(t_a-t_p\right)^4, \end{aligned} \tag{5}$$

where R_0, R_p, k_2 and k_4 are expressed as

$$\begin{cases} R_0=2R_p=2\sqrt{\left(r_p-r_a\right)^2+H^2} \\ k_2=\frac{r_ar_p\omega^2}{R_p} \\ k_4=-\left(\frac{r_ar_p\omega^4}{12R_p}+\frac{r_a^2r_p^2\omega^4}{4R_p^3}\right) \end{cases}, \tag{6}$$

where the coefficients k_2 and k_4 denote the range curvature and higher order phase coupling term, and R_0 is the minimum slant range between the target and the antenna phase center.

Assume that the radar transmits a linear frequency modulated (LFM) signal, then the received baseband echo signal of the point target after demodulation is

$$\begin{aligned} S_1(t_r;t_a) = w_r\left[t_r-\frac{2R\left(t_a;r_p\right)}{c}\right]w_a(t_a)exp\left[j\pi K_r\left(t_r-\frac{2R\left(t_a;r_p\right)}{c}\right)^2\right] \\ \times exp\left[-j\frac{4\pi}{\lambda}R\left(t_a;r_p\right)\right] \end{aligned}, \tag{7}$$

where $w_r(\cdot)$ and $w_a(\cdot)$ are range and azimuth envelopes, respectively, t_r denotes the range fast time variable, λ is the wavelength, K_r is the frequency modulation factor, and c is the speed of light.

3. Fast Imaging Algorithm for Helicopter-Borne RoASAR Based on 2-D CZT

In Section 2, the RoASAR geometry and signal model were presented, and some system parameters selection criteria were discussed. Based on that, the detailed derivations of the proposed fast RoASAR imaging algorithm using the 2-D CZT is now provided, which mainly contains the following three steps: (1) the precise 2-D frequency analytic expression, (2) spatial-variant RCM correction using an efficient, improved ICZT, and (3) SAR image azimuth distortion caused by the Deramp operation compensated by the CZT.

3.1. 2-D Spectrum Derivation Based on MSR

Due to the quartic item of $\left(t_a-t_p\right)$ in Equation (5), it is difficult to obtain the exact solution of the stationary phase point when the POSP is used to obtain the 2-D spectrum. In this paper, an MSR algorithm is introduced to derive the accurate 2-D spectrum analytic expression. After substituting Equations (5) and (6) into Equation (7) and using MSR (the detailed process of MSR is developed in Appendix B), the obtained accurate 2-D spectrum analytic expression is

$$S_2(f_r;f_a) = W_r(f_r)W_a(f_a)\cdot exp\left(-2\pi f_at_p\right)\cdot exp[j\Phi(f_r;f_a)], \tag{8}$$

where the phase term $\Phi(f_r;f_a)$ is expressed as

$$\Phi(f_r;f_a) = -\frac{2\pi(f_r+f_c)}{c}R_0-\frac{\pi f_r^2}{K_r}+\frac{\pi c}{2k_2(f_r+f_c)}f_a^2-\frac{\pi c^3k_4}{2k_2^4(f_r+f_c)^3}f_a^4, \tag{9}$$

where f_r is the range frequency, f_a is the azimuth frequency and f_c is the carrier frequency. According to Equation (7), the range frequency and the azimuth frequency domain are coupled together, and expanding the phase term in Equation (9) as a power series of f_r yields

$$\Phi(f_r; f_a) = \phi_0(f_a; R_0) + \phi_1(f_a; R_0) f_r + \phi_2(f_a; R_0) f_r^2 + \phi_3(f_a; R_0) f_r^3, \tag{10}$$

where

$$\begin{cases} \phi_0(f_a; R_0) = -\frac{2\pi f_c R_0}{c} + \frac{\pi c}{2k_2 f_c} f_a^2 - \frac{\pi c^3 k_4}{8k_2^4 f_c^3} f_a^4 \\ \phi_1(f_a; R_0) = -\frac{2\pi R_0}{c} - \frac{\pi c}{2k_2 f_c^2} f_a^2 + \frac{3\pi c^3 k_4}{8k_2^4 f_c^4} f_a^4 \\ \phi_2(f_a; R_0) = -\frac{\pi}{K_r} + \frac{\pi c}{2k_2 f_c^3} f_a^2 - \frac{3\pi c^3 k_4}{4k_2^4 f_c^5} f_a^4 \\ \phi_3(f_a; R_0) = -\frac{\pi c}{2k_2 f_c^4} f_a^2 + \frac{5\pi c^3 k_4}{4k_2^4 f_c^6} f_a^4 \end{cases}, \tag{11}$$

where $\phi_0(f_a; R_0)$ is the range-independent azimuth modulation term, $\phi_1(f_a; R_0)$ is the RCM term, $\phi_2(f_a; R_0)$ is the second range compression (SRC) term, and $\phi_3(f_a; R_0)$ is the cubic cross-coupling term. Due to the range-dependent characteristic of the RCM term, it is impossible to perform a precise range compression for all of the targets located in different range cells. In order to obtain accurate range processing, an efficient improved ICZT algorithm is developed.

3.2. Range Processing

Because the image quality is seriously affected by the inaccurate range processing, it is necessary to analyze the characteristics of the range and azimuth coupling terms. In the 2-D frequency domain, it is inconvenient to analyze three variables at the same time. In order to better illustrate the range-dependent feature of SRC and cubic coupling terms, f_a and f_r in Equation (11) are replaced by $B_a/2$ and $B_r/2$, respectively, and the approximated expression of which has only one variable R_0 that is derived as follows:

$$\begin{aligned} \Delta\phi_2 &= \left|\phi_2(f_a; R_0) f_r^2\right| \approx \phi_2\left(\tfrac{B_a}{2}; R_0\right) \cdot \left(\tfrac{B_r}{2}\right)^2 \\ \Delta\phi_3 &= \left|\phi_3(f_a; R_0) f_r^3\right| \approx \phi_3\left(\tfrac{B_a}{2}; R_0\right) \cdot \left(\tfrac{B_r}{2}\right)^3 \end{aligned} \tag{12}$$

where B_a is the Doppler bandwidth and B_r is the transmitted signal bandwidth.

From Section 2, the RoASAR simulation parameters are listed in Table 1. Using Equation (12), the range-dependent characteristic curves of SRC and cubic terms are shown in Figure 5a,b. It is seen that the variation is far less than $\pi/4$ and their range-dependent effect can be neglected in the range processing.

Table 1. Simulation Parameters.

Parameters Name	Value
Rotator length	2 m
Rotating angle speed	15 rad/s
Platform altitude	1000 m
Transmit bandwidth	300 MHz
Carrier frequency	10 GHz
Pulse repetition frequency	10 kHz
Reference slant range	2000 m
Azimuth beam width	80°
Scene size (range*azimuth)	700 m*70°

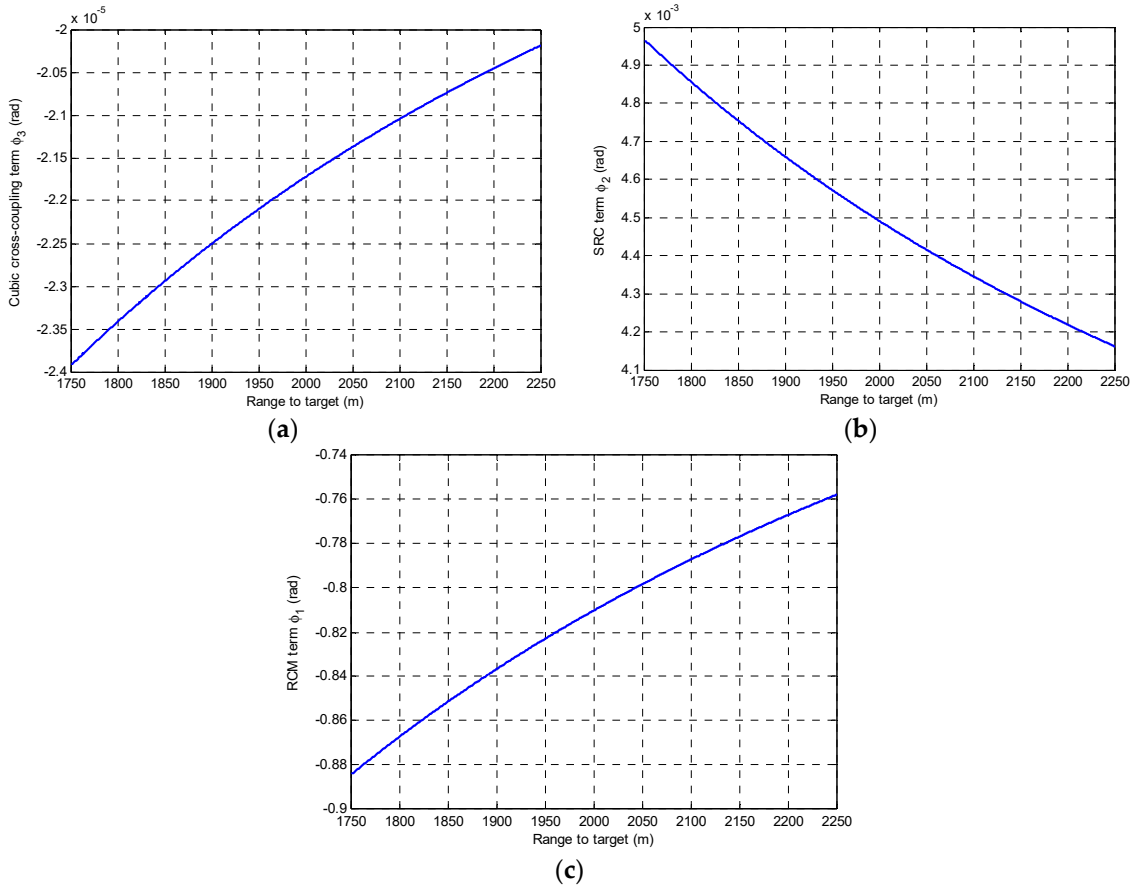

Figure 5. Range-dependent characteristic curves versus slant range. (**a**) Cubic cross-coupling term ϕ_3. (**b**) SRC term ϕ_2. (**c**) RCM term ϕ_1.

From Figure 5c, the RCM term varies greatly. The final imaging result will be affected if it is ignored. Therefore, in order to obtain accurate focusing result, an improved ICZT method is proposed to correct range spatial-variant RCM in this paper.

According to the aforementioned analysis, the SRC and cubic cross-coupling terms can be compensated with the reference distance, and one builds a compensate function as follows:

$$H_1(f_r; f_a; R_S) = exp\left[-j\phi_3(f_a; R_S)f_r^3 - j\phi_2(f_a; R_S)f_r^2\right], \tag{13}$$

where R_S is the reference distance between the center of the scene and the phase center of the radar, and the 2-D signal expression after compensation is

$$S_{3,1}(f_r; f_a) = W_r(f_r)W_a(f_a)\cdot exp\left(-2\pi f_a t_p\right)exp[j\phi_0(f_a; R_0) + j\phi_1(f_a; R_0)f_r]. \tag{14}$$

Since the RCM term cannot be ignored directly, the traditional Omega-k algorithm involves interpolation operations, but it increases the computational complexity. In this paper, an efficient improved ICZT is adopted to correct the RCM [17–19]. The RCM term $\phi_1(f_a; R_0)$ is decomposed into two parts: One related to the scene reference distance and another related to the variation distance. By introducing a range variation term $\Delta R = R_0 - R_s$, the RCM term $\phi_1(f_a; R_0)$ can be rewritten as

$$\phi_1(f_a; R_0) = R_s\frac{\phi_1(f_a; R_s)}{R_0} + \Delta R\frac{\phi_1(f_a; R_0)}{R_0}. \tag{15}$$

First, we compensate the bulk RCM term with the reference distance of the scene. The corresponding compensation function $H_{bulk}(f_r; f_a; R_s)$ is used to compensate the bulk RCM term. The expression of the compensation function is

$$H_{bulk}(f_r; f_a; R_s) = exp\left(-jR_s \frac{\phi_1(f_a; R_s) f_r}{R_0}\right). \tag{16}$$

The compensated 2-D signal is expressed as

$$S_{3,2}(f_r; f_a) = W_r(f_r) W_a(f_a) \cdot exp\left(-2\pi f_a t_p\right) exp\left[j\phi_0(f_a; R_0) + j\Delta R \frac{\phi_1(f_a; R_0) f_r}{R_0}\right]. \tag{17}$$

According to $2\Delta R f_r = \Delta R^2 + f_r^2 - (f_r - \Delta R)^2$, the first-order range term related to ΔR is decomposed as

$$\begin{array}{c} exp\left(j\Delta R \frac{\phi_1(f_a;R_0) f_r}{R_0}\right) = exp\left(j\frac{\phi_1(f_a;R_0)}{R_0}\frac{\Delta R^2}{2}\right) exp\left(j\frac{\phi_1(f_a;R_0)}{R_0}\frac{f_r^2}{2}\right) \\ \times exp\left(-j\frac{\phi_1(f_a;R_0)}{R_0}\frac{(f_r-\Delta R)^2}{2}\right) \end{array}. \tag{18}$$

The echo signal obtained by range inverse Fourier transform along the range frequency f_r is

$$\begin{array}{c} S_3(f_r; f_a; R_s) = \int S_{3,2}(f_r; f_a) exp\left[-j\Delta R \frac{\phi_1(f_a;R_s) f_r}{R_s}\right] df_r \\ = exp\left(-j\frac{\phi_1(f_a;R_s)}{R_s}\frac{\Delta R^2}{2}\right) \times \int S_{3,2}(f_r; f_a) \\ \times exp\left(-j\frac{\phi_1(f_a;R_s)}{R_s}\frac{f_r^2}{2}\right) exp\left(j\frac{\phi_1(f_a;R_s)}{R_s}\frac{(f_r-\Delta R)^2}{2}\right) df_r \end{array}. \tag{19}$$

In Equation (19), the exponential term unrelated to f_r is removed from the integral and R_0 is replaced by R_s (because R_s has little influence on the error), and it is simplified as

$$\begin{array}{c} S_3(f_r; f_a; R_S) = exp\left(-j\frac{\phi_1(f_a;R_s)}{R_S}\frac{\Delta R^2}{2}\right) \\ \times \left\{\left[S_{3,2}(f_r; f_a) exp\left(-j\frac{\phi_1(f_a;R_s)}{R_s}\frac{f_r^2}{2}\right)\right] \bigotimes exp\left(j\frac{\phi_1(f_a;R_s)}{R_s}\frac{f_r^2}{2}\right)\right\} \end{array}. \tag{20}$$

Obviously, Equation (20) is a process of ICZT after expansion. By use of twice phase multiplications and one convolution operation, the expression of the range Doppler domain of the signal is

$$S_{ICZT}(t_r; f_a) = w_r\left(t_r - \frac{R_0}{c}\right) W_a(f_a) \cdot exp\left(-2\pi f_a t_p\right) exp[j\phi_0(f_a; R_0)]. \tag{21}$$

From Equation (21), we can see that the range migration factor is equalized to be in unity after the ICZT operation, which means that the range spatial RCM is completely removed. Then, the azimuth processing can be applied to compress the azimuth modulated term.

3.3. Azimuth Processing

The Doppler centroid frequency of the target varies with the azimuth position under the wide azimuth beam. Standard SPECAN algorithm cannot obtain good focusing images in azimuth direction through Deramp processing and fast Fourier transform (FFT) [20]. The output of direct FFT in a standard SPECAN algorithm after the Deramp processing is

$$S_{specan}(t_r; f_a) = w_r\left(t_r - \frac{R_0}{c}\right) w_a\left(\pi \frac{F_a}{N_a}\left(f_a - \frac{2r_a\left(r_p - r_a\right)\omega^2}{\lambda R_0} t_p\right)\right) \cdot exp\left(-j\frac{2\pi R_0}{\lambda}\right). \tag{22}$$

Assume that the number of azimuth samples is N_a and the time domain output sample spacing is

$$\Delta t = \frac{prf}{N_a \cdot K_a}, \tag{23}$$

where prf is the pulse repetition frequency, then K_a is the azimuth frequency modulation factor, which varies with range, which results in uneven spacing of output samples and distortion in final imaging results. Its expression is as follows

$$K_a = \frac{r_a\left(r_p - r_a\right)\omega^2}{\lambda R_0}, \tag{24}$$

In general, image distortion is tolerable if the distance r_p varies within a small range. But for the RoASAR system which operates at low altitudes, the distance r_p changes rapidly as the beam moves from the edge to the center. In addition, because Δt is proportional to R_0, target located at near range are elongated, and it is compressed at far range. Therefore, the non-uniform spacing sampling of azimuth will seriously affect the image quality.

The efficient CZT uses the scaling Fourier transform (SCFT), instead of the Fourier transform, to solve the non-uniform sampling problem [21–24]. The compression factor is

$$\beta = \frac{R_s}{R_0} \cdot \frac{\left(r_p - r_a\right)}{r_s}, \tag{25}$$

where $r_s = \sqrt{R_s^2 - H^2}$ represents the reference ground position.

The scaling factor is a function of range and requires performing a scaling operation at each range gate. After the scaling operation, the output sampling interval of each distance gate is uniform, and thus, an accurate focusing image can be obtained.

First, we remove the high-order phase term from the range processing result, and then replace the hyperbolic phase with the quadratic phase. The compensation function needed is

$$H_2(t_r; f_a; R_0) = exp[-j\Delta\phi_0(f_a; R_0)], \tag{26}$$

where

$$\Delta\phi_0(f_a; R_0) = -\frac{\pi c^3 k_4}{8k_2^4 f_c^3} f_a^4. \tag{27}$$

After multiplying the range processing results of Equation (21) by (26), we transform the remaining signals into the time domain, given by

$$S_4(t_r; t_a) = w_r\left(t_r - \frac{R_0}{c}\right) w_a(t_a) exp\left(-\frac{2\pi R_0}{\lambda}\right) exp\left[-j\pi \frac{2r_a\left(r_p - r_a\right)\omega^2}{\lambda R_0}\left(t_a - t_p\right)^2\right]. \tag{28}$$

Based on the SPECAN algorithm, the Deramp processing is performed, and the azimuth-to-Deramp function is used to eliminate the quadratic phase. The Deramp function expression is

$$H_3(t_r; t_a; R_0) = exp\left(j\pi \frac{2r_a\left(r_p - r_a\right)\omega^2}{\lambda R_0}\left(t_a - t_p\right)^2\right). \tag{29}$$

Next, we propose to transform the signal into the range-Doppler domain by CZT to avoid interpolation. The kernel expression of CZT is

$$h_{CZT} = exp\left(-j2\pi \frac{1}{\beta} f_a t_a\right). \tag{30}$$

The final focusing image obtained is given by

$$\begin{aligned} S_{CZT}(t_r; f_a) &= SCFT\{S_4(t_r; t_a) \cdot H_4\} \\ &= w_r\left(t_r - \tfrac{R_0}{c}\right) w_a\left(\pi \tfrac{F_a}{N_a}\left(\tfrac{f_a}{\beta} - \tfrac{2r_a r_s \omega^2}{\lambda R_s} t_p\right)\right) exp\left(-\tfrac{2\pi R_0}{\lambda}\right). \end{aligned} \tag{31}$$

The flowchart of the whole algorithm is shown in Figure 6.

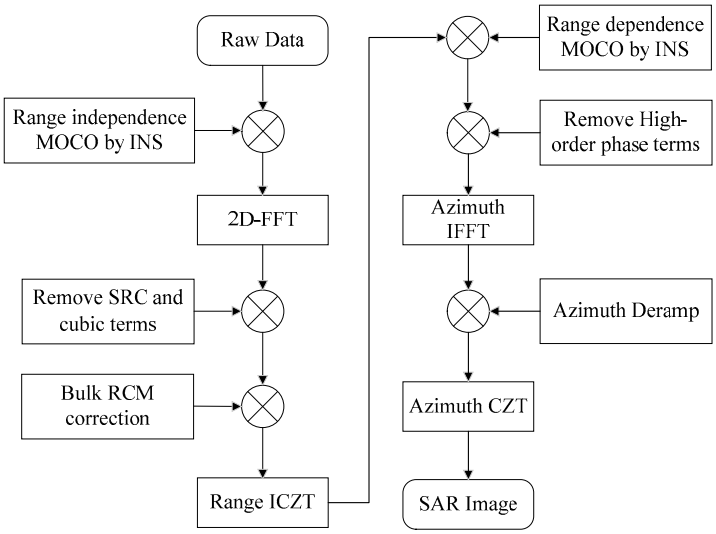

Figure 6. The flowchart of the algorithm presented in this paper.

3.4. Some Considerations of the Proposed Method in Applications

We now compare the computational complexity of our proposed method with the BP algorithm in [6] and Omega-k algorithm in [13]. The proposed algorithm avoids interpolation, and all the operations in the algorithm are realized by FFT and complex phase multiplications, which means it is of high efficiency. To be specific, we estimate the floating-point operations (FLOPs) of aforementioned algorithms. Generally speaking, an N-point FFT or inverse FFT (IFFT) need $5N\log_2(N)$ FLOPs, and $6N$ FLOPs are needed for one-time complex multiplication. Suppose that the range sample number is N_r, the azimuth sample number is N_a and the length of the interpolator kernel is N_{ker}. In this case, the computational complexity of BP algorithm in [6] is

$$C_{\mathrm{BP}} = 10N_aN_r\log_2(N_r) + 6N_aN_r + N_aN_r\left(10N_aN_r\log_2(N_r) + 6N_aN_r\right). \tag{32}$$

The computational load in terms of FLOPs for the Omega-k method in [13] is

$$C_{\mathrm{Omega-k}} = 20N_aN_r\log_2(N_r) + 20N_aN_r\log_2(N_a) + 18N_aN_r + 2(2N_{ker} - 1)N_aN_r. \tag{33}$$

According to the flowchart of the proposed method in Figure 6, the computational load of the proposed method is mainly composed of the following steps. First, the 2-D frequency is obtained by 2D-FFT and the computational complexity is $5N_aN_r\log_2(N_r) + 5N_aN_r\log_2(N_a)$ FLOPs. In range processing, the bulk RCM, SRC and cubic cross-coupling terms are compensated with the reference distance, directly, and the computational complexity is $6N_aN_r$ FLOPs. Then, the range-dependent RCM term is removed by using an ICZT operation, which contains twice phase multiplications and one convolution operation. The computational complexity is $10N_aN_r\log_2(N_r) + 18N_aN_r$ FLOPs. In azimuth processing, the implemented procedure mainly includes twice phase multiplications, one FFT and one CZT. In these steps, the computational complexity is $15N_aN_r\log_2(N_a) + 30N_aN_r$ FLOPs. To

summarize, we combine the complex multiplication together, and the total computation load in terms of FLOPs for the proposed method is approximately expressed as

$$C_{\text{proposed}} = 15N_aN_r\log_2(N_r) + 20N_aN_r\log_2(N_a) + 36N_aN_r. \quad (34)$$

It is noted that the BP and Omega-k algorithms that contain the correlation operation point-by-point and interpolations operation, respectively, have a higher computational load than the proposed algorithm, which means the proposed algorithm is more suitable to real-time imaging processing.

The motion errors generated from the atmospheric turbulence and platform tremble are contributing factors in the most airborne platforms, particularly in helicopter-borne RoASAR systems. The two-step approach in [25] and [26] is a common airborne motion compensation algorithm and can be easily integrated with the proposed 2-D CZT algorithm. First, the phase error correction for a reference range is defined and then it is carried out directly with range uncompressed data. Second, the phase error correction of range dependence is defined, which is carried out after the range cell migration correction (RCMC). In our system, the motion compensation step is also fused in the proposed method that can reduce the effects of the caused errors, depicted in Figure 6. Moreover, the data-driven autofocusing techniques in [8,9] are also good candidate methods for the helicopter-borne RoASAR motion compensation, and its will be our future study.

4. Simulation Results and Analysis

In this section, simulation results are presented to demonstrate the effectiveness and performance of the proposed algorithm for high resolution helicopter-borne RoASAR, where the simulated data processing parameters are the same scene as the original data in Table 1. For fairness of comparison, no weighting window and sidelobe control approach are adopted here. A circular imaging region with twenty-five targets is adopted, as shown in Figure 7. To compare the performance, the results of the BP algorithm in [6], Omega-k method [13], and SPECAN algorithm in [20] are also provided.

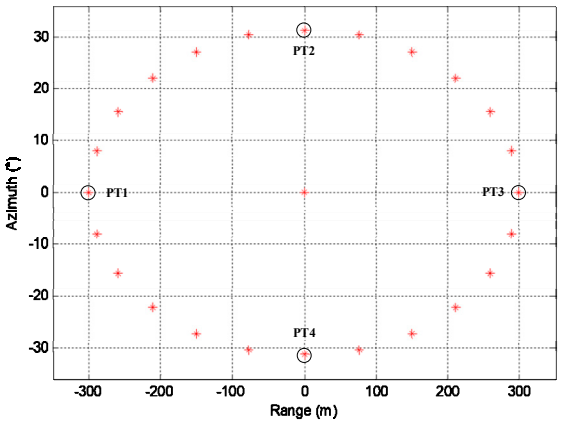

Figure 7. Imaging scene distribution.

For the edge points of the imaging scene, the results of the bulk range compensated echo with the phase of the reference point and the ICZT results proposed in this paper are respectively shown in Figure 8. It can be seen from Figure 8a,b that the RCM is well corrected by ICZT, and the main energy is well concentrated into one range gate.

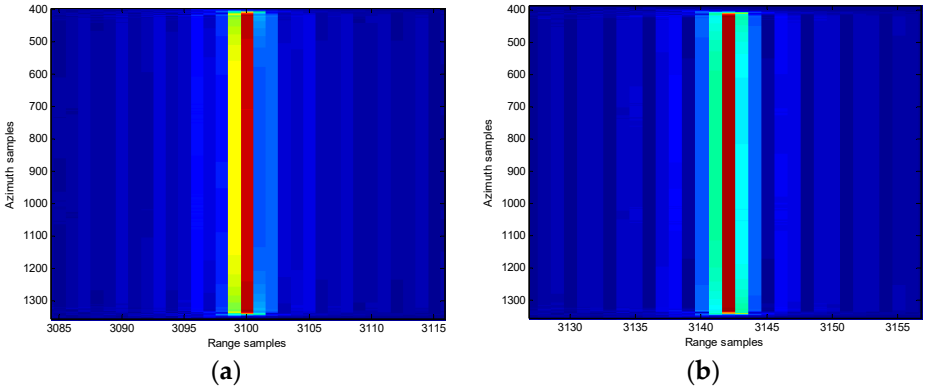

Figure 8. (**a**) Edge point range cell migration (RCM) result by bulk range compensation. (**b**) Edge point RCM correction result by inverse chirp-z transform (ICZT).

Meanwhile, to demonstrate the effectiveness of the proposed algorithm, the comparisons with the BP algorithm in [6], Omega-k algorithm in [13] and SPECAN algorithm in [20] are also provided. The imaging result of the BP algorithm and the Omega-k algorithm is depicted in Figure 9a,b. Both of them obtained a well-focused image, but suffering from a great computational load due to the time-domain correlation point-by-point and Stolt interpolation operation, respectively, which are not suitable for real-time imaging processing. The standard SPECAN algorithm adopts the azimuth Deramp operation, which ignores the influence of the range coupling term on the position modulation frequency, and the imaging result is depicted in Figure 9c. The imaging result shows an obvious sector shaped distortion, which is inconsistent with the original actual scene. The image result obtained by the proposed algorithm is shown in Figure 9d. It can be seen that the sector distortion caused by the Deramp operation has been well corrected, verifying the correctness and effectiveness of the proposed algorithm.

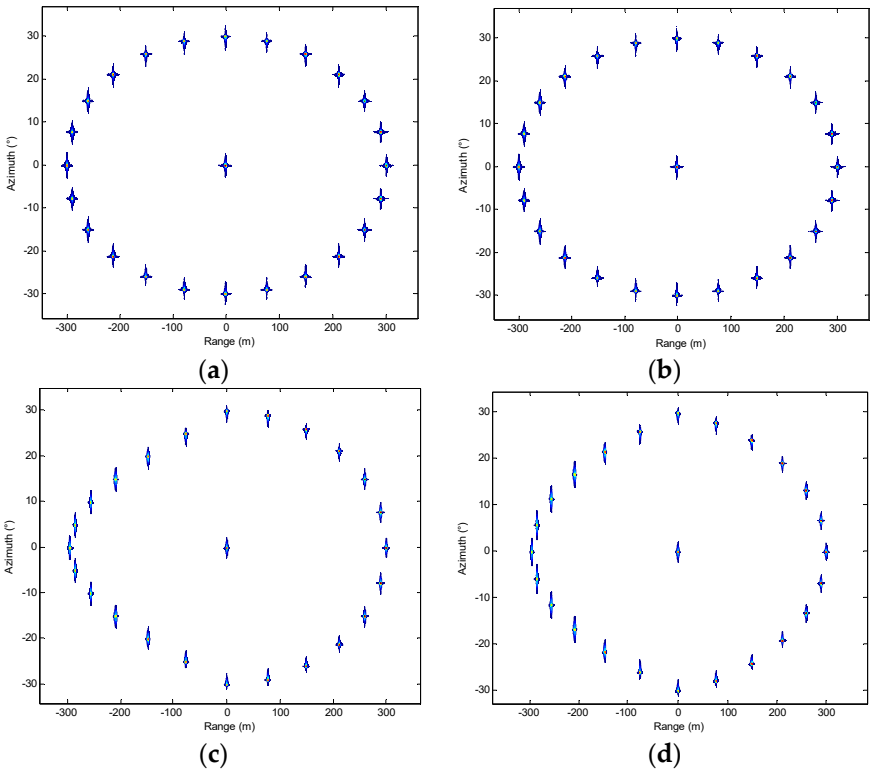

Figure 9. Comparison of the image results. (**a**) Back-projection (BP) algorithm in [6]. (**b**) Omega-k algorithm in [13]. (**c**) SPECAN algorithm in [20]. (**d**) Result by the proposed method.

To further demonstrate the performance of the proposed imaging algorithm, we present the magnified edge point target imaging results comparison in Figure 10. The range and azimuth profile of the BP algorithm and the Omega-k algorithm are depicted in Figure 10a–d, respectively. And the range and azimuth profile of the proposed method is provided in Figure 10e,f. It can be found that, from Figure 10, the well-focused SAR image can be obtained with the three methods.

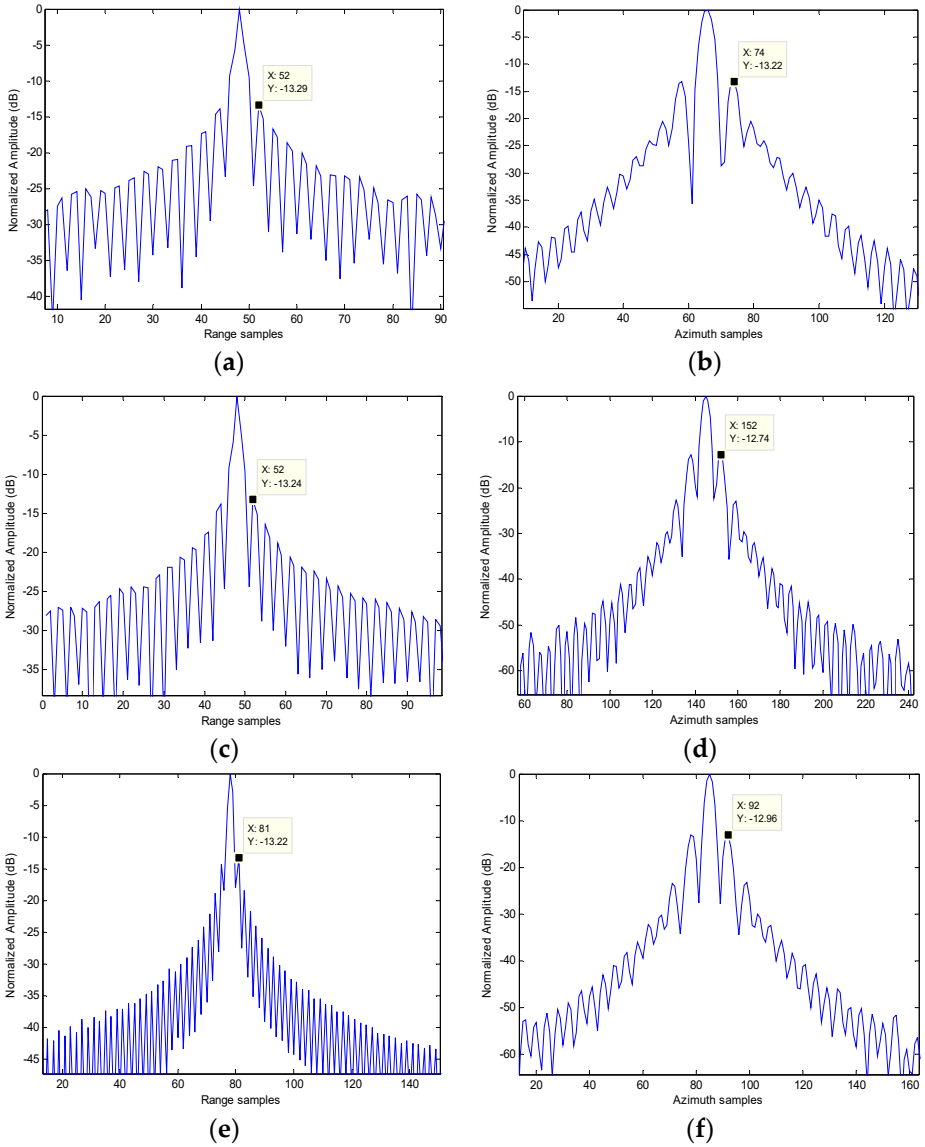

Figure 10. Magnified point target imaging results comparison. (**a**) Range profile of the BP algorithm. (**b**) Azimuth profile of the BP algorithm. (**c**) Range profile of the Omega-k algorithm. (**d**) Azimuth profile of the Omega-k algorithm. (**e**) Range profile of our proposed method. (**f**) Azimuth profile of our proposed method.

The performance measures include displacement, integral sidelobe ratio (ISLR), peak sidelobe ratio (PSLR) and resolution, and are shown in Tables 2 and 3. The true positions of targets are provided in Figure 7. It can be seen that the imaging accuracy of our algorithm is higher than the standard SPECAN algorithm, but slightly lower than the traditional time-domain algorithm and Omega-k algorithm. The comparison of imaging quality shows the effectiveness of proposed algorithm. However, the proposed method has the advantage in computational complexity without interpolation operation.

Table 2. Measurement of point displacement.

Approach	Range Displacement (m)				Azimuth Displacement (°)			
	PT1	PT2	PT3	PT4	PT1	PT2	PT3	PT4
BP	−0.24	0	+0.25	0	0	−0.053	0	+0.055
Omega-k	−0.24	0	+0.25	0	0	−0.055	0	+0.059
SPECAN	−0.52	0	+0.23	0	0	−0.110	0	+0.109
Proposed method	−0.25	0	+0.25	0	0	−0.057	0	+0.061

Table 3. Evaluation of the imaging performance.

Approach	Range			Azimuth		
	PSLR (dB)	ISLR (dB)	Resolution (m)	PSLR (dB)	ISLR (dB)	Resolution (°)
BP	−13.29	−9.76	0.55	−13.22	−9.72	0.1154
Omega-k	−13.24	−9.69	0.59	−12.74	−9.68	0.1263
Proposed method	−13.22	−9.68	0.59	−12.96	−9.64	0.1290
theoretical	−13.4	−9.80	0.50	−13.4	−9.80	0.1117

In Figure 11, the running times of different approaches versus imaging scene size are presented, where we used an Intel quad-core processor, CPU clocked frequency at 3.2 GHz, memory of 8 GB, and a Windows 10 operating system. It confirms that the computational times of the proposed method and the Omega-k algorithm are much less than the BP algorithm. And the computational cost of the proposed method is less than the Omega-k algorithm, since the interpolation operation is avoided, which is also consistent with the theoretical analysis. As the size of RoASAR imaging scene increases, the advantage of the proposed method in terms of running time is more obvious. To conclude, the proposed method can provide a high-resolution imaging result for helicopter-borne RoASAR, with a fast-computational speed in comparison with the BP algorithm in [6], fast factorized back-projection (FFBP) algorithm in [7], and Omega-k algorithm in [13]. This again demonstrates the proposed method is a promising candidate for practical applications.

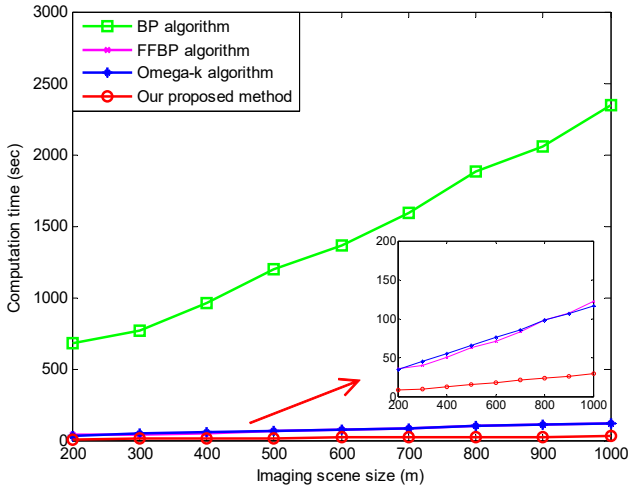

Figure 11. The running times versus RoASAR imaging scene size.

5. Conclusions

Aiming at solving the problems of limited azimuth resolution and high computational complexity of a helicopter RoASAR system, an improved 2-D CZT imaging algorithm is proposed. Based on the fourth-order expansion of instantaneous slant range, the approximated phase equation of slant range tolerates a larger azimuth reconstruction angle, and thus, the azimuth resolution is improved. The improved ICZT is used to eliminate RCM, where FFT in the standard SPECAN algorithm is

replaced, which avoids the interpolation operation to eliminate the sector distortion and reduces the computational complexity. Finally, simulation results are provided to verify the effectiveness of the algorithm.

Author Contributions: M.Q. and D.L. proposed the method, conceived and designed the experiments, and analyzed the data; X.T. and C.Z. performed the experiments and wrote the paper; and W.L. and L.X. revised the paper.

Funding: This work was funded by the National Key R&D Program of China (grant no. 2016YFE0200400), by the National Natural Science Foundation of China (grant no. 61771015 and 61801294), by the Graduate Scientific Research and Innovation Foundation of Chongqing (grant no. CYS19019), by the Key R&D Program of ShanXi Province (grant no. 2017KW-ZD-12), by the Innovative Research Group of National Natural Science Foundation of China (grant no. 61621005), by the Chongqing Research Program of Basic Research and Frontier Technology(cstc2018jcyjAX0351), by the Shanghai Aerospace Science and Technology Innovation Fund (grant no. SAST2017041), by the Guangxi Key Laboratory of Wireless Wideband Communication and Signal Processing, the 2017 Fund Project of the Director (grant no. GXKL06170202), and by the Fundamental Research Funds for the Central Universities (grant no. 2019CDQYTX012).

Acknowledgments: The authors would like to thank all the anonymous reviewers and editors for their useful comments and suggestions that greatly improved this paper.

Conflicts of Interest: The authors declare no conflict of interest.

Appendix A

We now give a detailed derivation process of the Taylor series expansion. The mathematical expression of the Taylor series expansion is as follows.

$$f(x) = \sum\nolimits_{n=0}^{\infty} \frac{f^{(n)}(x)}{n!}(x-x_0)^n\Big|_{x=x_0}. \tag{A1}$$

Based on (A1), the instantaneous slant range can be expressed as

$$R(t_a) \approx R(t_P) + \frac{R^{(1)}\big(t_p\big)\big(t_a-t_p\big)}{1!} + \frac{R^{(2)}\big(t_p\big)\big(t_a-t_p\big)^2}{2!} + \ldots \frac{R^{(n)}\big(t_p\big)\big(t_a-t_p\big)^n}{n!}\Bigg|_{t_a=t_P}. \tag{A2}$$

where

$$R(t_a) = \sqrt{{r_p}^2 + {r_a}^2 + H^2 - 2r_a r_p \cos\omega\big(t_a-t_p\big)}. \tag{A3}$$

The first derivative of instantaneous slant range is

$$R^{(1)}(t_a) = \frac{r_a r_p \omega \sin\omega\big(t_a-t_p\big)}{\sqrt{{r_p}^2 + {r_a}^2 + H^2 - 2r_a r_p \cos\omega\big(t_a-t_p\big)}} = \frac{\omega r_a r_p \sin\omega\big(t_a-t_p\big)}{R(t_a)}. \tag{A4}$$

Similarly, the second derivative of instantaneous slant range is

$$R^{(2)}(t_a) = \frac{\omega^2 r_a r_p \cos\omega\big(t_a-t_p\big)}{R(t_a)} - \frac{\omega^2 {r_a}^2 {r_p}^2 \sin^2\omega\big(t_a-t_p\big)}{R^3(t_a)}. \tag{A5}$$

The third derivative of instantaneous slant range is

$$\begin{aligned} R^{(3)}(t_a) = &-\frac{\omega^3 r_a r_p \sin\omega\big(t_a-t_p\big)}{R(t_a)} - \frac{3\omega^3 {r_a}^2 {r_p}^2 \sin\big[\omega\big(t_a-t_p\big)\big]\cos\big[\omega\big(t_a-t_p\big)\big]}{R^3(t_a)} \\ &+\frac{3\omega^3 {r_a}^3 {r_p}^3 \sin^3\omega\big(t_a-t_p\big)}{R^5(t_a)}. \end{aligned} \tag{A6}$$

Finally, the fourth derivative of instantaneous slant range is

$$\begin{aligned} R^{(4)}(t_a) &= -\frac{\omega^4 r_a r_p \cos\omega(t_a-t_p)}{R(t_a)} - \frac{3\omega^4 {r_a}^2 {r_p}^2 \cos[\omega(t_a-t_p)] - 4\omega^4 {r_a}^2 {r_p}^2 \sin[\omega(t_a-t_p)]}{R^3(t_a)} \\ &= \frac{18\omega^4 {r_a}^3 {r_p}^3 \sin^2[\omega(t_a-t_p)]\cos[\omega(t_a-t_p)]}{R^5(t_a)} - \frac{15\omega^4 {r_a}^4 {r_p}^4 \sin^4\omega(t_a-t_p)}{R^7(t_a)}. \end{aligned} \tag{A7}$$

When $t_a = t_P$, the instantaneous slant range and their derivatives are

$$\begin{aligned} R(t_P) &= \sqrt{{r_p}^2 + {r_a}^2 + H^2} \\ R^{(1)}(t_P) &= 0 \\ R^{(2)}(t_P) &= \frac{\omega^2 r_a r_p}{R(t_P)} \\ R^{(3)}(t_P) &= 0 \\ R^{(4)}(t_P) &= -\frac{\omega^4 r_a r_p}{R(t_P)} - \frac{3\omega^4 {r_a}^2 {r_p}^2}{R^3(t_P)}. \end{aligned} \tag{A8}$$

Using the results obtained, the second-order approximation of instantaneous slant range is given in (A9), where the approximation error is corresponding to Figure 4a in the paper.

$$R(t_a) \approx R(t_P) + \frac{1}{2}\frac{r_a r_p \omega^2}{R(t_P)}\left(t_a - t_p\right)^2. \tag{A9}$$

And the fourth-order approximation of instantaneous slant range is given in (A10), where the approximation error is corresponding to Figure 4b in the paper.

$$\begin{aligned} R(t_a) &\approx R(t_P) + \tfrac{1}{2}\frac{r_a r_p \omega^2}{R(t_P)}\left(t_a - t_p\right)^2 + \tfrac{1}{24}\left(-\frac{\omega^4 r_a r_p}{R(t_P)} - \frac{3\omega^4 {r_a}^2 {r_p}^2}{R^3(t_P)}\right)\left(t_a - t_p\right)^4 \\ &= R(t_P) + \frac{r_a r_p \omega^2}{2R(t_P)}\left(t_a - t_p\right)^2 - \left(\frac{\omega^4 r_a r_p}{24R(t_P)} - \frac{\omega^4 {r_a}^2 {r_p}^2}{8R^3(t_P)}\right)\left(t_a - t_p\right)^4. \end{aligned} \tag{A10}$$

Using (A10), the fourth-order Taylor series expansion of two-way slant range can be expressed as Equation (5) in the article.

Appendix B

The MSR approach was originally developed in [16]. Based on the idea of MSR, the point target signal in the time domain after range compression is

$$S_1(t_r; t_a) = w_r\left[t_r - \frac{2R\left(t_a; r_p\right)}{c}\right] w_a(t_a) exp\left[-j\frac{4\pi}{\lambda}R\left(t_a; r_p\right)\right]. \tag{A11}$$

The fourth-order approximation of instantaneous slant range is

$$2R\left(t_a; r_p\right) = R_0 + k_2\left(t_a - t_p\right)^2 + k_4\left(t_a - t_p\right)^4, \tag{A12}$$

where the derivation of the coefficients is given in the previous response

$$\begin{cases} R_0 = 2R_p = 2\sqrt{\left(r_p - r_a\right)^2 + H^2} \\ k_2 = \frac{r_a r_p \omega^2}{R_p} \\ k_4 = -\left(\frac{r_a r_p \omega^4}{12R_p} + \frac{r_a^2 r_p^2 \omega^4}{4R_p^3}\right) \end{cases}. \tag{A13}$$

Expanding the point target signal up to the fourth azimuth frequency terms, the 2-D point target spectrum is given by

$$S_2(f_r;t_a) = W_r(f_r)w_a(t_a)exp\left[-j2\pi\frac{(f_r+f_c)2R\left(t_a;r_p\right)}{c}\right]. \tag{A14}$$

Next, we perform an azimuth FT. Using the method of stationary phase, azimuth frequency is related to azimuth time by

$$\left(-\frac{c}{f_r+f_c}\right)f_a = 2k_2\left(t_a-t_p\right)+4k_4\left(t_a-t_p\right)^3. \tag{A15}$$

We can derive an expression of t_a in terms of f_a by using the series reversion. Using the results in the Appendix in reference [16], we arrive at

$$t_a(f_a)-t_p = A_1\left(-\frac{c}{f_r+f_c}f_a\right)+A_2\left(-\frac{c}{f_r+f_c}f_a\right)^2+A_3\left(-\frac{c}{f_r+f_c}f_a\right)^3, \tag{A16}$$

where

$$\begin{aligned} A_1 &= (2k_2)^{-1} \\ A_2 &= 0 \\ A_3 &= (2k_2)^{-5}(0-2k_2{\cdot}4k_4). \end{aligned} \tag{A17}$$

Substituting (A16) to (A14), we obtain the 2-D spectrum of $S_1(t_r;t_a)$, given by

$$S_3(f_r;f_a) = W_r(f_r)W_a(f_a){\cdot}exp\left(-2\pi f_a t_p\right){\cdot}exp[j\Phi(f_r;f_a)], \tag{A18}$$

where the phase term $\Phi(f_r;f_a)$ is expressed as

$$\Phi(f_r;f_a) = -\frac{2\pi(f_r+f_c)}{c}R_0-\frac{\pi f_r^2}{K_r}+\frac{\pi c}{2k_2(f_r+f_c)}f_a^2-\frac{\pi c^3k_4}{2k_2^4(f_r+f_c)^3}f_a^4. \tag{A19}$$

References

1. Kreitmair-Steck, W.; Wolframm, A.P. Heliradar-a Rotating Antenna Synthetic Aperture Radar for Helicopter all Weather Operations. In Proceedings of the AGARD 59th Guidance and Control Panel, Pratica di Mare, Italy, 20–25 October 1994; pp. 56–62.
2. Joelianto, E.; Budiyono, A.; Wijayanti, I.E.; Megawati, N.Y. Model Predictive Control for Obstacle Avoidance as Hybrid Systems of Small Scale Helicopter. In Proceedings of the 2013 3rd International Conference on Instrumentation Control and Automation, Ungasan, Indonesia, 28–30 August 2013.
3. Kwag, Y.K.; Kang, J.W. Obstacle Awareness and Collision Avoidance Radar Sensor System for Low-Altitude Flying Smart UAV. In Proceedings of the 23rd Digital Avionics Systems Conference, Salt Lake City, UT, USA, 28–28 October 2004.
4. Kreitmair, W. Heliradar: The Pilot's Eye for Flights in Adverse Weather Conditions. In *SPIE 1995 Aerosense Symposium*; Enhanced and Synthetic Vision: Orlando, FL, USA, 1995.
5. Guo, H.D.; Li, X.W. Characteristics and application expansion of new generation SAR earth observation technology. *Chin. Sci. Bull.* **2011**, *56*, 1155–1168. [CrossRef]
6. Jakowatz, C.V., Jr.; Wahl, D.E.; Yocky, D.A. Beamforming as a Foundation for Spotlight-Mode SAR Image Formation by Backprojection. In Proceedings of the SPIE-The International Society for Optical Engineering, Orlando, FL, USA, 15 April 2008; Volume 6970.
7. Ulander, L.M.; Hellsten, H.; Stenstrom, G. Synthetic-aperture radar processing using fast factorized back-projection. *IEEE Trans. Aerosp. Electron. Syst.* **2003**, *39*, 760–776. [CrossRef]

8. Zhang, L.; Li, H.-L.; Qiao, Z.-J.; Xing, M.D.; Bao, Z. Integrating Autofocus Techniques with Fast Factorized Back-Projection for High-Resolution Spotlight SAR Imaging. *IEEE Geosci. Remote Sens. Lett.* **2013**, *10*, 1394–1398. [CrossRef]
9. Zhou, S.; Yang, L.; Zhao, L.; Bi, G. Quasi-Polar-Based FFBP Algorithm for Miniature UAV SAR Imaging Without Navigational Data. *IEEE Trans. Geosci. Remote Sens.* **2017**, *55*, 7053–7065. [CrossRef]
10. Chen, S.B.; Chun-sheng, J.L. Operation mode of circular trace scanning SAR for wide observation. *J. Electron. Inf. Technol.* **2008**, *30*, 2805–2808.
11. Li, D.; Liao, G.S.; Xu, Q.; Wang, W. High resolution imaging algorithm for helicopter-borne rotating synthetic aperture radar. *J. Syst. Eng. Electron.* **2013**, *35*, 1389–1395.
12. Zhang, J.; Liao, G.S.; Xu, J.W.; Yang, K.; Zhu, S. Research on high resolution wavenumber-domain imaging algorithm for ROSAR. *J. Syst. Eng. Electron.* **2017**, *39*, 1127–1234.
13. Li, D.; Liao, G.; Yang, L. Modified Omega-K algorithm for processing helicopter-borne frequency modulated continuous waveform rotating synthetic aperture radar data. *J. Syst. Eng. Electron.* **2015**, *26*, 476–485. [CrossRef]
14. Adams, J.W.; Bayma, R.W.; Lawrence, M.E.; Petrosian, L. On the modified chirp z transform for synthetic aperture radar systems. *IEEE Trans. Signal Process.* **1991**, *39*, 953–955. [CrossRef]
15. Li, D.; Liu, H.; Liao, Y.; Gui, X. A Novel Helicopter-Borne Rotating SAR Imaging Model and Algorithm Based on Inverse Chirp-Z Transform Using Frequency-Modulated Continuous Wave. *IEEE Geosci. Remote Sens. Lett.* **2015**, *12*, 1–5.
16. Neo, Y.L.; Wong, F.; Cumming, I.G. A two-dimensional spectrum for bistatic SAR processing using series reversion. *IEEE Geosci. Remote Sens. Lett.* **2007**, *4*, 93–96. [CrossRef]
17. Lanari, R. A new method for the compensation of the SAR range cell migration based on the chirp-z transform. *IEEE Trans. Geosci. Remote Sens.* **1995**, *33*, 1296–1299. [CrossRef]
18. Zhou, P.; Zhou, S.; Xiong, T.; Li, Y.C.; Xing, M.D. A chirp-z transform imaging algorithm for missile-borne SAR with diving maneuver based on the method of series reversion. *J. Electron. Inf. Technol.* **2010**, *32*, 2861–2867. [CrossRef]
19. Li, C.; He, M. Imaging algorithm for geosynchronous orbit SAR based on chirp-z transform and azimuth scaling. *J. Electron. Inf. Technol.* **2015**, *37*, 1736–1742.
20. Cumming, I.G.; Wong, F.H. *Digital Processing of Synthetic Aperture Radar Data*, 2nd ed.; Artech House: Norwood, MA, USA, 2005; pp. 249–260.
21. Yang, W.; Chen, J.; Zeng, H.; Wang, P.; Liu, W. A wide-swath spaceborne TOPS SAR image formation algorithm based on chirp scaling and chirp-z transform. *Sensors* **2016**, *16*, 2095. [CrossRef] [PubMed]
22. Zhong, H.; Zhang, Y.; Chang, Y.; Liu, E.; Tang, X.; Zhang, J. Focus High-Resolution Highly Squint SAR Data Using Azimuth-Variant Residual RCMC and Extended Nonlinear Chirp Scaling Based on a New Circle Model. *IEEE Geosci. Remote Sens. Lett.* **2018**, *15*, 547–551. [CrossRef]
23. Bi, H.; Zhang, B.; Zhu, X.; Hong, W. Azimuth-range decouple-based L 1 regularization method for wide ScanSAR imaging via extended chirp scaling. *J. Appl. Remote Sens.* **2017**, *11*, 15007. [CrossRef]
24. Wu, Y.; Sun, G.-C.; Xia, X.-G.; Xing, M.; Yang, J.; Bao, Z. An Azimuth Frequency Non-Linear Chirp Scaling (FNCS) Algorithm for TOPS SAR Imaging with High Squint Angle. *IEEE J. Sel. Top. Appl. Earth Obs. Remote Sens.* **2014**, *7*, 213–221.
25. Su, Y.X.; Li, D. Motion compensation and imaging algorithm for helicopter-borne rotating synthetic aperture radar. *Radar Sci. Technol.* **2018**, *16*, 383–390.
26. Xing, M.; Jiang, X.; Wu, R.; Zhou, F.; Bao, Z. Motion Compensation for UAV SAR Based on Raw Radar Data. *IEEE Trans. Geosci. Remote Sens.* **2009**, *47*, 2870–2883. [CrossRef]